electronics

MDPI

Article

Adaptive Fault Diagnosis of DC-DC Boost Converters in Photovoltaic Systems Based on Sliding Mode Observers with Dynamic Thresholds

Maouadda Ismail [1], Karim Dahech [1], Fernando Tadeo [2,*], Tarak Damak [1] and Mohamed Chaabane [1]

[1] Laboratory of Sciences and Techniques of Automatic Control and Computer Engineering (Lab-STA), National School of Engineering of Sfax (ENIS), University of Sfax, BP 1173, Sfax 3038, Tunisia; ismail.maouadda@enis.tn (M.I.); karim.dahech@isgis.usf.tn (K.D.); tarak.damak@enis.tn (T.D.); mohamed.chaabane@enis.tn (M.C.)

[2] Institute of Sustainable Processes, University of Valladolid, 47005 Valladolid, Spain

* Correspondence: fernando.tadeo@uva.es

Abstract

A robust methodology for parametric fault diagnosis in photovoltaic systems is proposed, focusing on DC-DC boost converters. The methodology uses Adaptive Sliding Mode Observers (ASMO) combined with adaptive thresholding. Specifically, an observer-based scheme detects and isolates faults in passive components of the converter, achieving complete isolation in about 0.05 s, even under varying environmental conditions. In addition, a dynamic fault discrimination approach is introduced, based on adaptive thresholds derived from Exponentially Weighted Moving Average (EWMA). This minimizes false alarms caused by transient conditions. Stability and robustness are guaranteed through Lyapunov-based conditions. Simulation results under sequential and simultaneous fault scenarios confirm rapid and precise fault detection, highly specific isolation, and exceptional resilience against environmental disturbances.

Keywords: photovoltaic systems; fault detection and isolation; DC-DC boost converter; adaptive sliding mode observer; Lyapunov stability; adaptive thresholds

1. Introduction

Global energy demand is increasing over time, leading to a rapid transition to renewable energy. Among these alternatives, photovoltaic electricity production can stand out as a clean and sustainable solution [1]. However, the expansion of solar energy on electrical grids is accompanied by an increased risk of malfunctions [2–4]. In this regard, DC/DC converters are important components in photovoltaic systems, due to their direct influence on the efficiency and stability of energy conversion [5,6].

The quick detection of component faults in DC-DC boost converter is essential to ensure converter protection [5]. These faults fall into three categories: switch failures such as open- and short-circuit conditions [5,7], passive or active component faults such as capacitor degradation or inductor variations [5], and sensor failures [5].

To address these issues, Fault Detection and Isolation (FDI) systems are employed [2]: fault detection involves a binary decision to determine whether a fault has occurred; then, fault identification follows to pinpoint the faulty component [2]. These systems can be categorized into model-based and model-free methods [2]. The model-based approaches use models (mathematical or analytical) to generate residuals that are then used to detect

Check for updates

Academic Editor: Francisco Javier Ruiz-Rodríguez

Received: 9 November 2025
Revised: 10 December 2025
Accepted: 20 December 2025
Published: 22 December 2025

Copyright: © 2025 by the authors. Licensee MDPI, Basel, Switzerland. This article is an open access article distributed under the terms and conditions of the Creative Commons Attribution (CC BY) license.

and isolate faults [8,9]. In contrast, model-free approaches rely on data-driven techniques and artificial intelligence, to construct systems that learn a system's behavior directly from data [4,10]. Despite their power, AI-based approaches frequently encounter limitations in these applications due to the need of large amounts of reliable data, and the significant computational requirements [4,10].

Several methods exist for diagnosing faults in DC-DC converters. Comprehensive monitoring systems, such as the one described in [11], provide online fault detection for switches, capacitors, and inductors using minimal sensors. Data driven approaches, like the Fuzzy Cerebellar Model Neural Network (FCMNN) in [12], employ pattern recognition via Fast Fourier Transform to identify component degradation. Integrated control-diagnosis schemes, as explored in [13], combine predictive control and fault detection using shared sensor measurements. Observer-based techniques include the Luenberger observer in [14], which isolates faults using specialized filters, and the parameter estimation method in [15], which analyzes startup data without requiring test signals. Despite these advances, key limitations persist: observer-based methods often require precise modeling and lack robustness to uncertainties; data-driven approaches depend on extensive training data; and many existing solutions struggle to adapt to varying environmental conditions a gap our method specifically addresses.

While existing methods provide valuable solutions, they present specific limitations that motivate this work. Luenberger observers [16], though effective for fault detection, are often sensitive to model uncertainties and require precise system modeling, which is challenging under real-world varying conditions. Similarly, data-driven approaches [4] demonstrate strong pattern recognition but heavily depend on extensive training datasets and significant computational resources, limiting their practicality in resource-constrained PV systems. To bridge this gap, we propose an Adaptive Sliding Mode Observer (ASMO) combined with an Exponentially Weighted Moving Average (EWMA)-based dynamic thresholding mechanism. This integrated approach uniquely addresses the shortcomings of prior methods by: (1) Integrating sliding mode robustness with online parameter adaptation, eliminating the need for large datasets. (2) Providing enhanced disturbance rejection through sliding mode injection and adaptive parameter estimation for gradual faults. (3) Employing dynamic thresholding that automatically adjusts to operating conditions, reducing false alarms under transients.

While this study focuses specifically on parametric faults in passive components such as inductors and capacitors, it is acknowledged that switching components like IGBTs and MOSFETs are also critical. Concentrating on passive components enables the development of a specialized methodology for gradual parametric degradation.

The main contributions of this paper are as follows:

- The development of an ASMO for robust state and parameter estimation in the presence of model uncertainties and external disturbances.
- The design of an adaptive threshold mechanism that dynamically adjusts to operating conditions, significantly reducing false alarms, and improving detection reliability.
- A comprehensive stability analysis using Lyapunov theory to guarantee the convergence and performance of the proposed observer.
- The validation under multiple fault scenarios and varying environmental conditions.

This paper is organized as follows. Section 2 presents the modeling of the photovoltaic system, including the PV generator and the DC-DC boost converter. Section 3 describes the design of the fault diagnostic scheme and presents the Adaptive Sliding Mode Observer used for fault detection. Section 4 details the adaptive thresholds proposed. Section 5 provides simulation results and analysis under different fault scenarios. Finally, Section 6 concludes the paper and outlines future work.

2. System Modeling

The photovoltaic system considered in this study comprises three principal elements: a photovoltaic generator, a DC-DC boost converter and a resistive load. The complete system configuration is depicted in Figure 1.

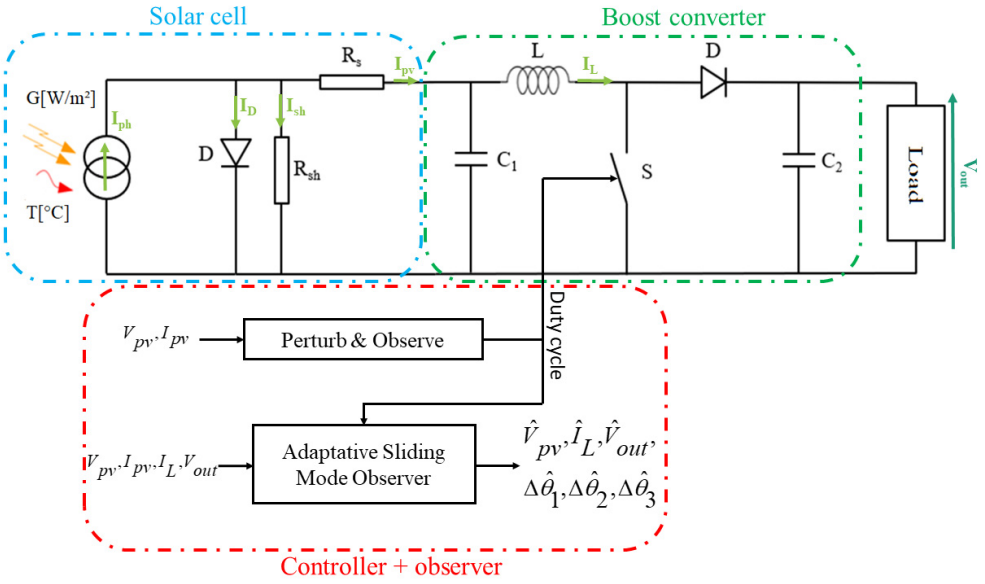


Figure 1. Schematic of the photovoltaic system with the designed ASMO-based observer.

2.1. PV Generator Model

The solar cell is represented by an equivalent circuit model including a photocurrent source I_{ph} proportional to the incident solar irradiance, a rectifying diode D, a shunt resistance R_{sh}, and a series resistance R_s. The output current of the PV cell is given by [17]:

$$I_{pv} = I_{ph} - I_D - I_{sh} \tag{1}$$

where:

$$I_{ph} = \left[I_{rs} - k_i\left(T - T_{ref}\right)\right]\frac{G}{G_{ref}} \tag{2}$$

$$I_D = I_0\left[e^{\frac{q\times(V_{pv}+R_s\times I_{pv})}{A\times K\times T}} - 1\right] \tag{3}$$

$$I_{sh} = \frac{V_{pv} + I_{pv}\times R_s}{R_{sh}} \tag{4}$$

In these equations, I_0 represents the reverse saturation current of the diode, T is the cell temperature, A is the diode ideality factor, K is the Boltzmann constant (1.38×10^{-23} J/K), and q is the elementary charge (1.602×10^{-19} C). As a result, the current-voltage (I_{pv}-V_{pv}) behavior of the solar cell is described by the following equation:

$$I_{pv} = I_{ph} - I_0\left(e^{\frac{q(V_{pv}+R_s\times I_{pv})}{K\times T\times A}} - 1\right) - \frac{V_{pv} + R_s\times I_{pv}}{R_{sh}} \tag{5}$$

2.2. DC-DC Boost Converter Model

2.2.1. Fault Free Model

In the absence of faults, the dynamics of the DC-DC boost converter are characterized by the subsequent state-space description obtained by Kirchhoff's laws [18]:

$$\begin{cases} \dot{V}_{pv} = \theta_1 (I_{pv} - I_L) \\ \dot{I}_L = \theta_2 (V_{pv} - (1-\alpha) V_{out}) \\ \dot{V}_{out} = \theta_3 \left((1-\alpha) I_L - \frac{V_{out}}{R} \right) \end{cases} \tag{6}$$

where

$$\theta_1 = \frac{1}{C_1}; \theta_2 = \frac{1}{L}; \theta_3 = \frac{1}{C_2} \tag{7}$$

where I_{pv} and V_{pv} are the PV current and voltage, respectively. I_L is the inductor current; V_{out} denotes the output voltage across the load; C_1 and C_2 corresponds to the input and output capacitances; L is the inductor; α refers to the duty cycle of the converter's switch; and θ_1, θ_2 and θ_3 are the model parameters.

2.2.2. Faulty Model

The methodology proposed focuses on parametric faults in passive components: capacitance degradation affecting θ_1 and θ_3 and inductor variation affecting θ_2. These faults lead to gradual parameter degradation, making them well suited for detection through observer-based techniques. In contrast, switch faults, such as open- and short-circuit conditions, necessitate complementary detection strategies so they are not considered in this work.

To address component failures, the nominal model (6) is augmented by incorporating additive parameter variations denoted $\Delta\theta_i$: In normal operation $\Delta\theta_i$ is zero, but under a fault it is not, changing the dynamic behavior of the system as described by the following representation:

$$\begin{cases} \dot{V}_{pv} = (\theta_1 + \Delta\theta_1)(I_{pv} - I_L) \\ \dot{I}_L = (\theta_2 + \Delta\theta_2)(V_{pv} - (1-\alpha) V_{out}) \\ \dot{V}_{out} = (\theta_3 + \Delta\theta_3) \left((1-\alpha) I_L - \frac{V_{out}}{R} \right) \end{cases} \tag{8}$$

A corresponding formulation of (8) can be expressed as follows:

$$\begin{cases} \dot{V}_{pv} = \theta_1 (I_{pv} - I_L) + \Delta\theta_1 (I_{pv} - I_L) \\ \dot{I}_L = \theta_2 (V_{pv} - (1-\alpha) V_{out}) + \Delta\theta_2 (V_{pv} - (1-\alpha) V_{out}) \\ \dot{V}_{out} = \theta_3 \left((1-\alpha) I_L - \frac{V_{out}}{R} \right) + \Delta\theta_3 \left((1-\alpha) I_L - \frac{V_{out}}{R} \right) \end{cases} \tag{9}$$

Therefore, the faulty model is given by the following matrix formulation:

$$\dot{X} = f(X, u) + g(X, u) \Delta\theta_n \tag{10}$$

where

$$X = \begin{bmatrix} V_{pv} & I_L & V_{out} \end{bmatrix}^T \tag{11}$$

$$u = \alpha \tag{12}$$

$$f(X, u) = \begin{bmatrix} \theta_1 (I_{pv} - I_L) \\ \theta_2 (V_{pv} - (1-\alpha) V_{out}) \\ \theta_3 \left((1-\alpha) I_L - \frac{V_{out}}{R} \right) \end{bmatrix} \tag{13}$$

$$g(X, u) = \begin{bmatrix} (I_{pv} - I_L) & 0 & 0 \\ 0 & (V_{pv} - (1-\alpha) V_{out}) & 0 \\ 0 & 0 & \left((1-\alpha) I_L - \frac{V_{out}}{R} \right) \end{bmatrix} \tag{14}$$

and

$$\Delta\theta_n = \begin{bmatrix} \Delta\theta_1 & \Delta\theta_2 & \Delta\theta_3 \end{bmatrix}^T \tag{15}$$

To optimize power transfer to the load, a Maximum Power Point Tracking (MPPT) controller is assumed. Specifically, a Perturb and Observe (P & O) algorithm adjusts the duty cycle α of the boost converter, based on the measurements of the photovoltaic current and voltage to ensure operation at the Maximum Power Point (MPP).

Although the presented models accurately describe the behavior of the PV system under normal and fault conditions, effective fault detection and isolation requires a robust diagnostic scheme. The following section presents the design of an adaptive sliding mode observer specifically developed to meet this requirement.

3. Design of the Fault Diagnostic Scheme

The proposed fault diagnosis scheme, illustrated in Figure 2, employs an Adaptive Sliding Mode Observer (ASMO) to detect and isolate parametric faults in the DC-DC boost converter. This architecture follows a conventional observer-based fault detection approach. The system processes an input signal, while its outputs may be altered in the presence of a fault. Simultaneously, an observer driven by the same input provides an estimate of the system's expected behavior. The difference between the measured outputs and the observer's estimated outputs, known as the residual, is compared against adaptive thresholds. When the residual signal exceeds the upper or the lower thresholds, a fault is indicated, and an alarm is activated.

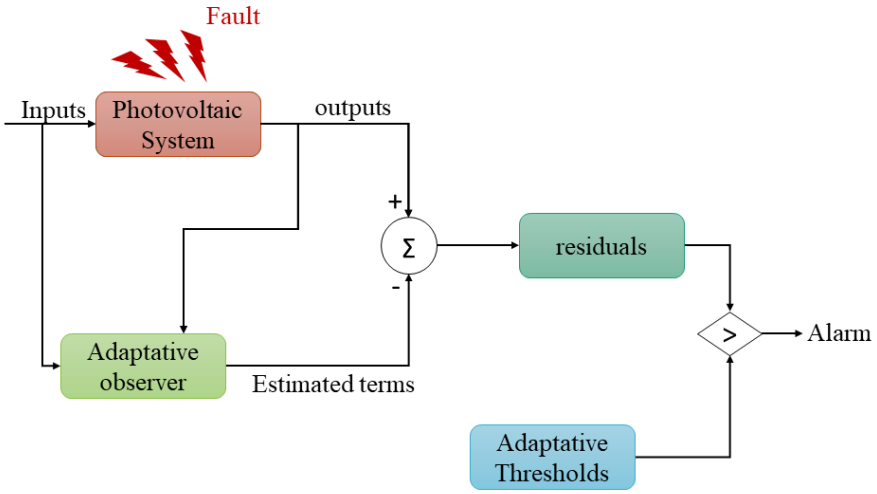


Figure 2. General schematic of the developed fault detection system.

3.1. Adaptive Sliding Mode Observer Design

In this section, the ASMO is developed to estimate the system states and parameters in the presence of faults. The observer includes three sliding surfaces denoted as e_1, e_2, and e_3. These surfaces respectively represent the error estimation for the PV voltage, the inductor current and the output voltage.

These sliding surfaces are defined as follows [19]:

$$\begin{cases} e_1 = \hat{V}_{pv} - V_{pv} \\ e_2 = \hat{I}_L - I_L \\ e_3 = \hat{V}_{out} - V_{out} \end{cases} \tag{16}$$

The mathematical formulation of the ASMO is expressed by the following equations:

$$\begin{cases} \dot{\hat{X}} = f(\hat{X}, u) + g(\hat{X}, u)\Delta\hat{\theta}_n + K_n\, sign(e_n) \\ \Delta\dot{\hat{\theta}} = g(\hat{X}, u)\Gamma_n\, sign(e_n) \end{cases} \tag{17}$$

where, $K_n = \begin{bmatrix} K_1 & K_2 & K_3 \end{bmatrix}^T$ denotes the observer gains, $\Gamma_n = \begin{bmatrix} \Gamma_1 & \Gamma_2 & \Gamma_3 \end{bmatrix}^T$ defines the adaptation gains and $e_n = \begin{bmatrix} e_1 & e_2 & e_3 \end{bmatrix}^T$ represents the estimation errors.

The observer equations can be extended as follows:

$$\begin{cases} \dot{\hat{V}}_{pv} = \theta_1(I_{pv} - \hat{I}_L) + \Delta\hat{\theta}_1(I_{pv} - \hat{I}_L) + K_1\, sign(e_1) \\ \dot{\hat{I}}_L = \theta_2(\hat{V}_{pv} - (1-\alpha)\hat{V}_{out}) + \Delta\hat{\theta}_2(\hat{V}_{pv} - (1-\alpha)\hat{V}_{out}) + K_2\, sign(e_2) \\ \dot{\hat{V}}_{out} = \theta_3\left((1-\alpha)\hat{I}_L - \frac{\hat{V}_{out}}{R}\right) + \Delta\hat{\theta}_3\left((1-\alpha)\hat{I}_L - \frac{\hat{V}_{out}}{R}\right) + K_3\, sign(e_3) \\ \Delta\dot{\hat{\theta}}_1 = \Gamma_1(I_{pv} - \hat{I}_L) sign(e_1) \\ \Delta\dot{\hat{\theta}}_2 = \Gamma_2(\hat{V}_{pv} - (1-\alpha)\hat{V}_{out})\, sign(e_2) \\ \Delta\dot{\hat{\theta}}_3 = \Gamma_3\left((1-\alpha)\hat{I}_L - \frac{\hat{V}_{out}}{R}\right) sign(e_3) \end{cases} \tag{18}$$

3.2. Stability Analysis

Theorem 1. *Consider the faulty DC-DC boost converter system defined by Equations (10)–(15), with the ASMO described by Equation (17). The estimation error is then given by:*

$$e_n = \hat{X}_n - X_n \tag{19}$$

$$\Delta\widetilde{\theta}_n = \Delta\theta_n - \Delta\hat{\theta}_n \tag{20}$$

where X is defined by Equation (11), and $\Delta\theta_n$ is given by Equation (15). $\hat{X}_n = \begin{bmatrix} \hat{V}_{pv} & \hat{I}_L & \hat{V}_{out} \end{bmatrix}$ and $\Delta\hat{\theta}_n = \begin{bmatrix} \Delta\hat{\theta}_1 & \Delta\hat{\theta}_2 & \Delta\hat{\theta}_3 \end{bmatrix}$ are the estimated values of X and $\Delta\theta_n$, respectively. Given that the functions $f(X,u)$ and $g(X,u)$ are Lipschitz continuous with positive constants L_f and L_g, and the observer gains K_i are selected to satisfy: $K_{\min} > \left(L_f + L_g\left\|\Delta\theta_n\right\|\right)\left\|e_n\right\| + \lambda$, for $\lambda > 0$, then the origin $\left(e, \Delta\widetilde{\theta}_n\right) = (0,0)$ of the error dynamics is stable, and the estimation errors converge to zero asymptotically.

Proof. Consider the following candidate Lyapunov function:

$$V = \frac{1}{2}e_n^T e_n + \frac{1}{2}\Delta\widetilde{\theta}_n^T\Gamma_n^{-1}\Delta\widetilde{\theta}_n \tag{21}$$

The time derivative of V is given by:

$$\dot{V} = e_n^T\dot{e}_n - \Delta\widetilde{\theta}_n^T\Gamma_n^{-1}\Delta\dot{\hat{\theta}}_n \tag{22}$$

Substituting $\dot{e}_n$ and $\Delta\dot{\hat{\theta}}_n$, the following result is obtained:

$$\dot{V} = e_n^T\left(\dot{X} - \dot{\hat{X}}\right) - \Delta\widetilde{\theta}_n^T.\Gamma_n^{-1}\,\Gamma_n\, g\left(\hat{X}, u\right) sign(e_n) \tag{23}$$

$$\begin{aligned} \dot{V} = {} & e_n^T\left[f(X,u) - f\left(\hat{X},u\right)\right] + \left[g(X,u) - g\left(\hat{X},u\right)\right]\Delta\theta_n \\ & + g\left(\hat{X},u\right)\Delta\widetilde{\theta}_n - K_n\, sign(e_n) - \Delta\widetilde{\theta}_n^T\, g\left(\hat{X},u\right) sign(e_n) \end{aligned} \tag{24}$$

By applying the Lipschitz properties:

$$\left\|f(X,u)-f(\hat{X},u)\right\| \leq L_f\left\|e_n\right\|, \quad \left\|g(X,u)-g(\hat{X},u)\right\| \leq L_g\left\|e_n\right\|$$

We derive the upper bound:

$$\dot{V} = L_f\left\|e_n\right\|^2 + L_g\left\|\Delta\theta_n\right\|\left\|e_n\right\|^2 - K_{\min}\left\|e_n\right\| \tag{25}$$

To ensure $\dot{V} \leq -\lambda\left\|e_n\right\|$, the following condition must be satisfied:

$$K_{\min} > L_f + L_g\left\|\Delta\theta_n\right\|\left\|e_n\right\| + \lambda \tag{26}$$

Consequently, $\dot{V}$ is negative definite, which confirms the stability of the observer error dynamics. □

4. Adaptive Thresholds

To improve the robustness of the proposed fault diagnosis scheme, an adaptive threshold approach based on the Exponentially Weighted Moving Average (EWMA) method is proposed. Unlike traditional fixed thresholds, this method dynamically adjusts the detection terminals according to the evolution of operating conditions. This makes it possible to effectively distinguish parametric faults from transient variations induced by changes in environmental conditions [20,21].

The principle is based on the recursive estimation of the mean μ and standard deviation σ of the estimation residuals $r_i = \Delta\hat{\theta}_i - \Delta\theta_i$ using the following EWMA equations [22]:

Mean update:

$$\mu_t = (1-\alpha)\mu_{t-1} + \alpha r_t\,, \quad t > 0 \tag{27}$$

Variance update:

$$\sigma_t^2 = (1-\alpha)\sigma_{t-1}^2 + \alpha(r_t-\mu_t)^2 \tag{28}$$

Then, the adaptive thresholds, upper and lower limits, are obtained by the subsequent equations:

$$J_{upper} = \mu_t + \lambda\sigma_t \text{ and } J_{lower} = \mu_t - \lambda\sigma_t \tag{29}$$

where α is the forgetting factor ($\alpha \in]0,1[$) and λ denotes the sensitivity coefficient (typically λ = 3).

Finally, the fault detection is triggered when:

$$F_{\text{det}} = \begin{cases} 1 \;\; if\, r_i < J_{lower} \;or\; r_i > J_{upper} \\ 0 \;\; otherwise \end{cases} \tag{30}$$

The EWMA threshold parameters were carefully selected based on established statistical principles and extensive preliminary testing. The sensitivity coefficient λ = 3, providing approximately 99.7% confidence bounds for normally distributed residuals. The forgetting factor α = 0.1 was chosen through systematic parameter sweeps to optimally balance noise rejection with fault sensitivity. Our analysis confirms that these parameters achieve the best compromise between detection performance and false-alarm prevention, validating our central claim of reliable fault diagnosis under varying operating conditions.

5. Simulation Results and Analysis

The fault diagnosis performance of a sliding mode observer was investigated through MATLAB/Simulink 2020b version. To assess the observer's robustness, additive Gaussian noise was injected into the output signals. The noise had zero mean and a variance of 0.000005. The random seed was set to 1 to ensure reproducible results.

The diagnostic framework was evaluated under parametric faults injected into critical components θ_1, θ_2 and θ_3. These faults were modeled as significant deviations from nominal values: a 10% decrease for $\Delta\theta_1$, a 7% decrease for $\Delta\theta_2$ this fault exhibits a characteristically slow, gradual decrease in parameter value, both at its onset near t = 1.1 s and its disappearance near t = 1.9 s, and a 10% decrease for $\Delta\theta_3$. The simulation was performed with a variable temperature profile. From 0 s to 1 s, the temperature was fixed at 20 °C. Then it was increased to 25 °C from 1 s to 2 s. Finally, it was set to 15 °C. The irradiation profile was also dynamic: it changed from 700 W/m^2 at t = 1 s to 1000 W/m^2, and then to 600 W/m^2 at t = 3 s. These variations were used to evaluate the algorithm's robustness under changing operating conditions. The parameters of the studied photovoltaic system and the synthesis parameters of the ASMO are gathered in Tables 1 and 2, respectively.

Table 1. Parameters of the photovoltaic system used for validation.

Parameters	Symbol	Value
Voltage at the maximum power point	V_{max}	27 V
current at the maximum power point	I_{max}	7.6 A
Maximum power	P_{max}	210 W
Open circuit voltage	V_{oc}	32.9 V
Short circuit current	I_{sc}	8.21 A
Input capacitor	C_1	10^{-3} F
Output capacitor	C_2	10^{-3} F
Inductor	L	1.21×10^{-3} H
Load	R	25 Ω

Table 2. Observer parameters used for validation.

Symbol	Value
K_1	50 V/s
K_2	100 A/s
K_3	500 V/s
Γ_1	10^6 1/F.A.s
Γ_2	10^6 1/H.V.s
Γ_3	10^6 1/F.A.s

The evaluation of the proposed scheme is conducted considering two scenarios.

First Scenario: All faults in a given period:

For the first test, three faults are injected independently. A fault is introduced in θ_1 during the interval [0.5 s, 0.9 s], followed by a fault in θ_2 during [1.2 s, 1.8 s], and finally in θ_3 during [2.1 s, 2.6 s], as shown in Figure 3.

The simulation results for the first operating scenario are presented in Figures 4–9. Figure 4 illustrates the time profile of $\Delta\theta_i$ faults and their estimations $\Delta\hat{\theta}_i$. The results demonstrate the remarkable ability of the ASMO to estimate faults. For each parameter, after a fault, the estimated value converges very quickly to the actual value and maintains an accurate estimation throughout the fault.

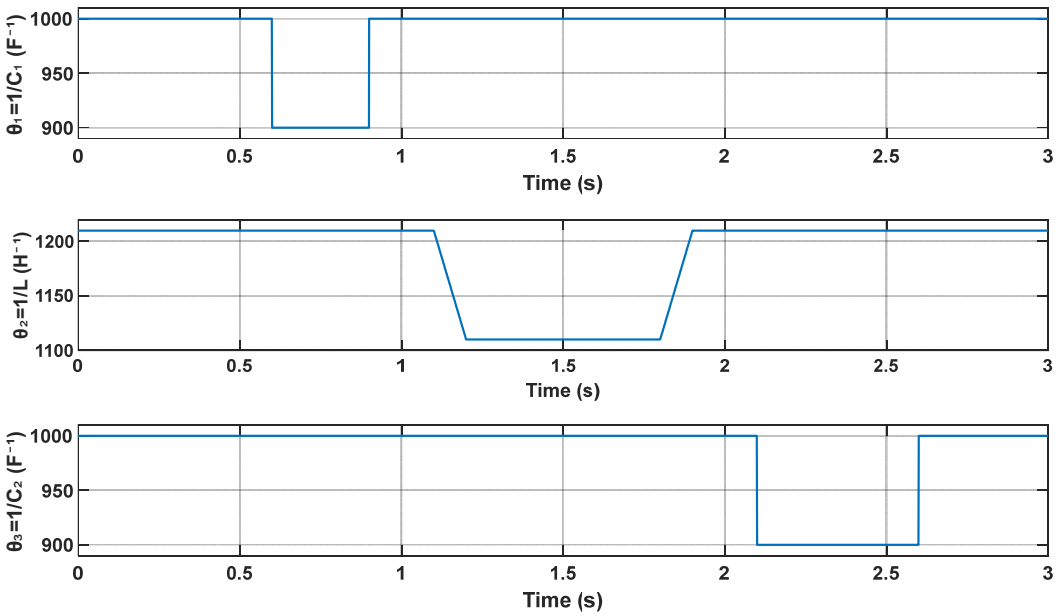


Figure 3. Injected faults in the first scenario.

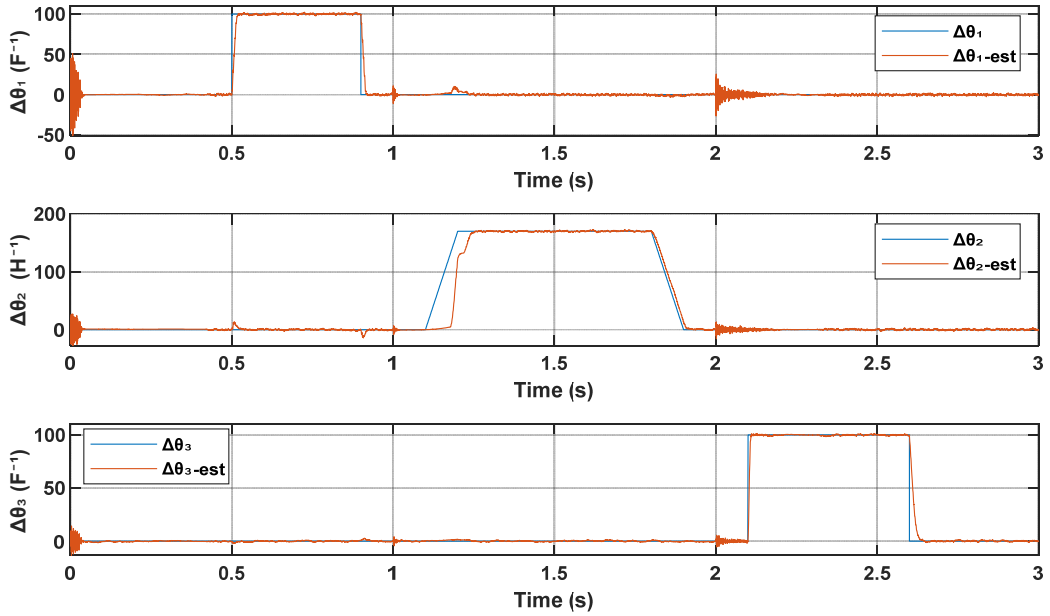


Figure 4. Comparative evolution of actual and estimated parameters in the first scenario.

Figures 5–7 reveal the dynamic behavior of the residuals r_i for each parameter. Under normal conditions, the residuals fluctuate around zero with minimal amplitude, forming a narrow noise band. Upon injection of each fault, the corresponding residual undergoes an immediate and significant discontinuity, clearly exceeding the background noise. Following this initial jump, the residuals converge to a new steady state value within approximately 0.05 s of fault occurrence, demonstrating the observer's rapid response. The characteristic step-like increase in residual amplitude occurs precisely during the injected fault intervals: for the first fault in θ_1 between t = 0.5 s and t = 0.9 s (Figure 5), for the second fault in θ_2 between t = 1.2 s and t = 1.8 s (Figure 6), and for the third fault in θ_3 between t = 2.1 s and t = 2.6 s (Figure 7). In contrast, changes in solar irradiance, which are applied at t = 1 s and t = 2 s, produce only minor, bounded perturbations to the residuals that do not cross the adaptive detection thresholds. The specificity of the response where only the residual of the faulty parameter reacts confirms the effective fault isolation.

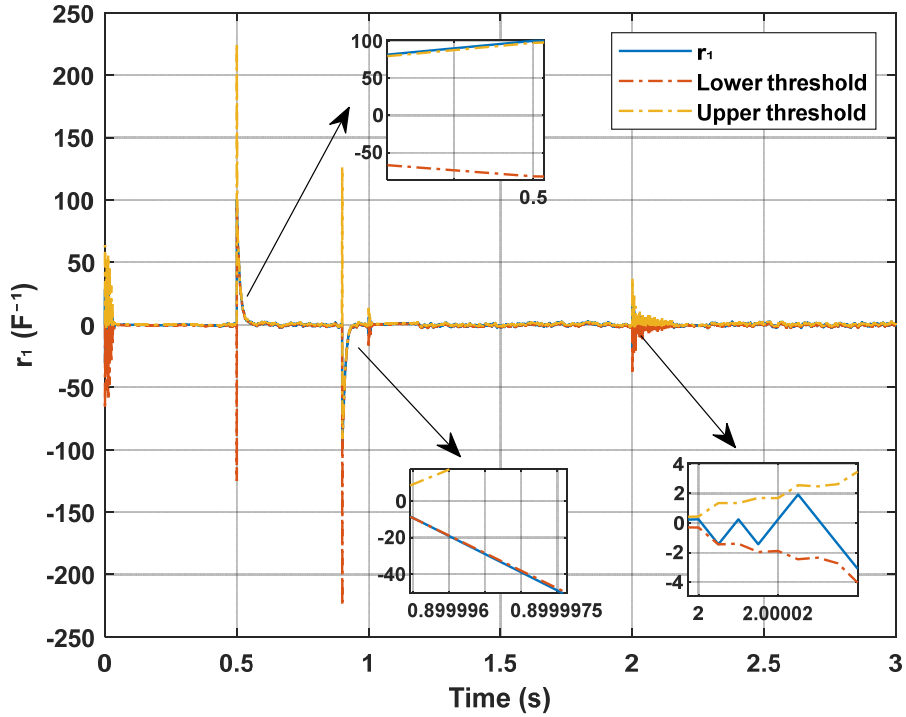


Figure 5. Residual signal of $\Delta\theta_1$ in the first scenario.

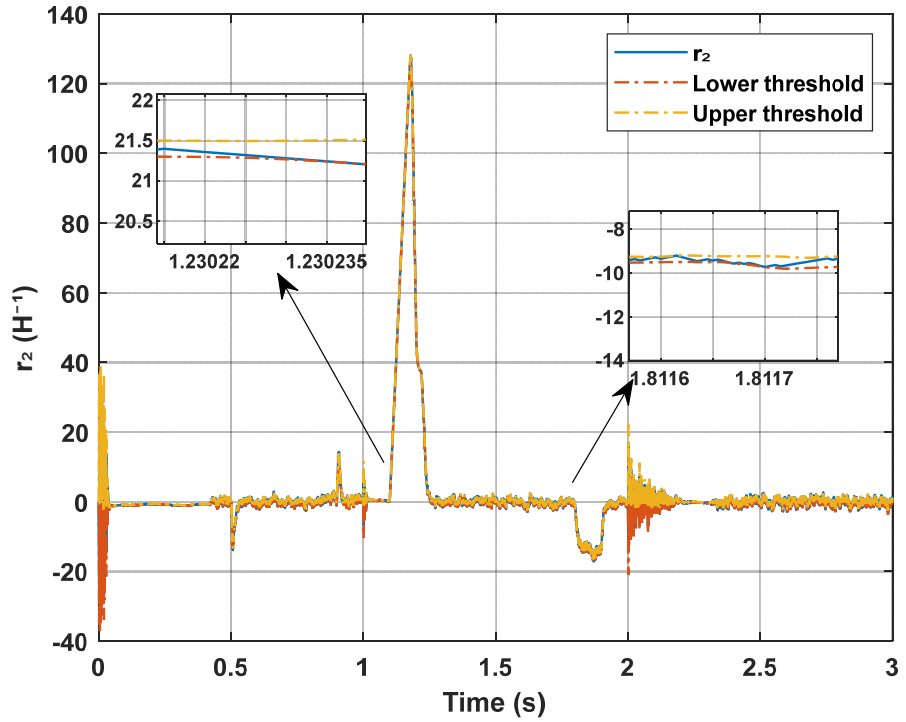


Figure 6. Residual signal of $\Delta\theta_2$ in the first scenario.

Figure 8 translates the residuals into a binary alarm: the alarm is exclusively activated during fault intervals, with sharp activations and deactivations that are synchronized with the faults. The complete absence of false alarms during irradiance transitions at t = 1 s and t = 2 s proves the robustness of the system to external disturbances, thanks to the integration of adaptive thresholds in the diagnostic mechanism.

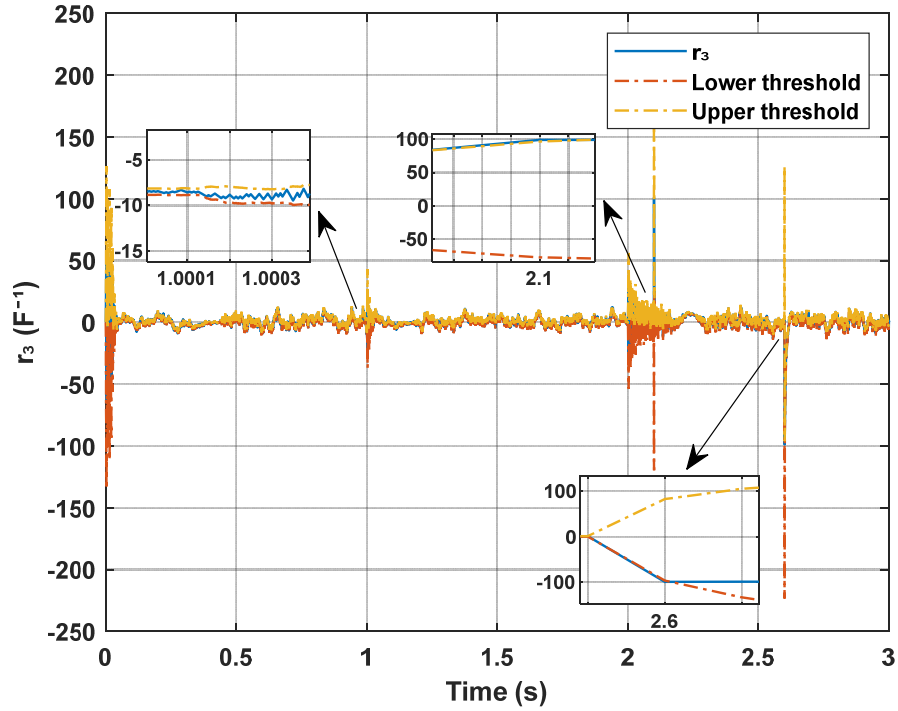


Figure 7. Residual signal of $\Delta\theta_3$ in the first scenario.

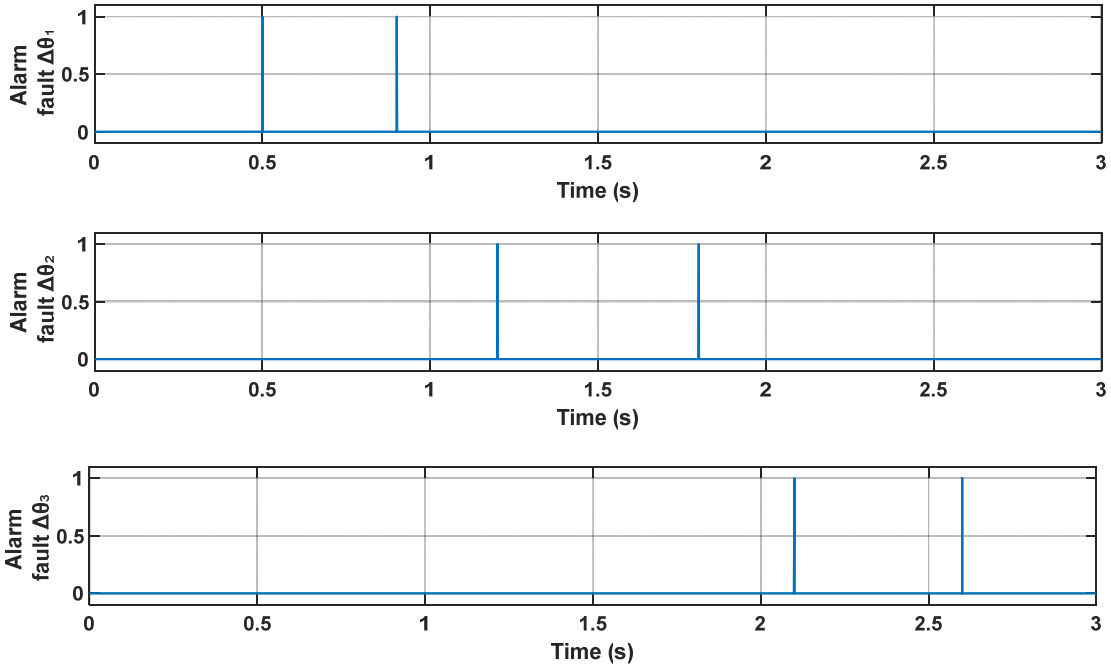


Figure 8. Fault detection signals in the first scenario.

Figure 9 shows the robustness and efficiency of the system. It can be confirmed that the control strategy ensures maximum power point operation, rapidly converging and stabilizing the output power at the optimal panel level, even in the presence of faults and external disturbances. It is noted that a disturbance occurs specifically at the time of irradiance variation; however, the resilience of the system is confirmed by its immediate and accurate return to the MPP.

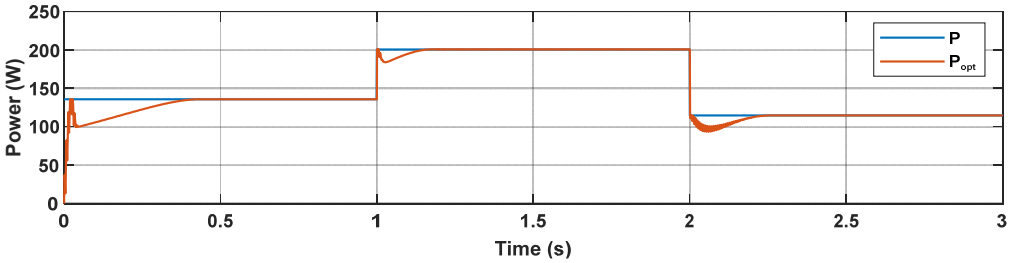


Figure 9. Evolution of PV power and its optimal value in the first scenario.

Scenarios 2: simultaneous multiple faults

The second test scenario involved the simultaneous injection of faults. A fault was introduced in θ_1 during the interval [0.6 s, 1.9 s], in θ_2 during [1.2 s, 2.1 s], and in θ_3 during [1.4 s, 2.6 s] as shown in Figure 10. Notably, the triple overlap period between 1.4 s and 1.9 s constitutes the ultimate test for the isolation capability of the algorithm.

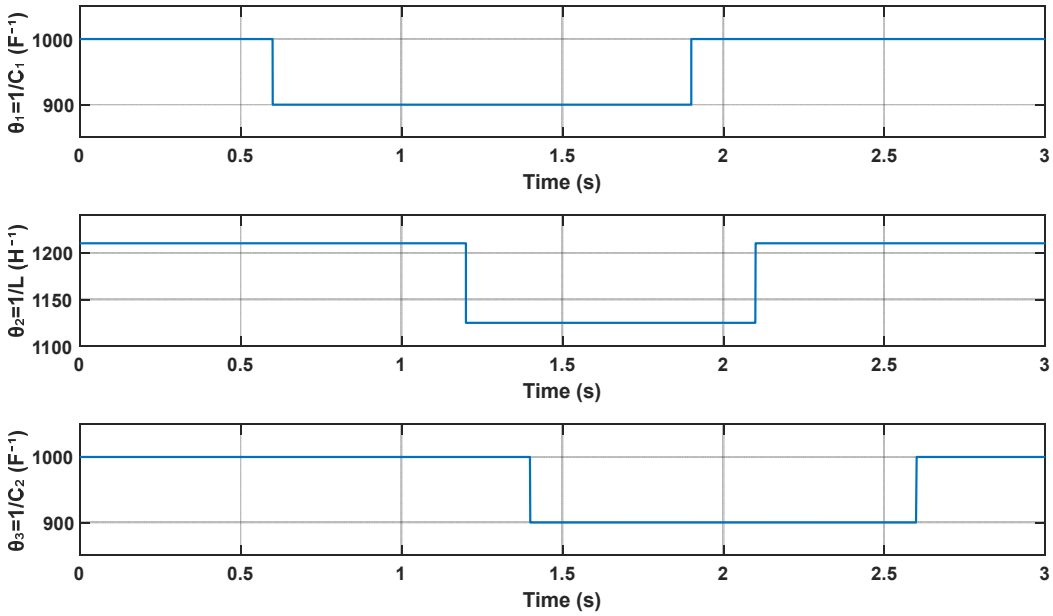


Figure 10. Fault injection profile for the second scenario.

Figures 11–16 show the simulation results corresponding to the second operating mode. Figure 11 demonstrates the discriminatory power of ASMO. Indeed, the observer manages to estimate all three parametric variations simultaneously and accurately, even during the period of complete overlap. The estimated trajectory follows tightly each individual defect without significant mutual interference.

The residual signals r_i, depicted in Figures 12–14, quantify the difference between the actual and estimated faults. These residuals remain close to zero in the absence of faults but become significantly disrupted when a fault is injected. Following each fault occurrence, the residuals converge to a steady state offset within about 0.05 s. The timing of these disruptions corresponds accurately to the injected fault intervals: for θ_1 between t = 0.6 s and t = 1.9 s (Figure 12), for θ_2 between t = 1.2 s and t = 2.1 s (Figure 13), and for θ_3 between t = 1.4 s and t = 2.6 s (Figure 14). Figure 12 confirms that this disruption immediately breaches the adaptive thresholds, generating a clear alarm signal. Thus, this methodology exhibits significant robustness against external perturbations. While variations in solar irradiance, introduced at t = 1 s and t = 2 s, induce oscillations, they are effectively ignored by the system, thus preventing false alarms. Simultaneously, the algorithm successfully detects the injected faults, proving its capability to isolate multiple failures.

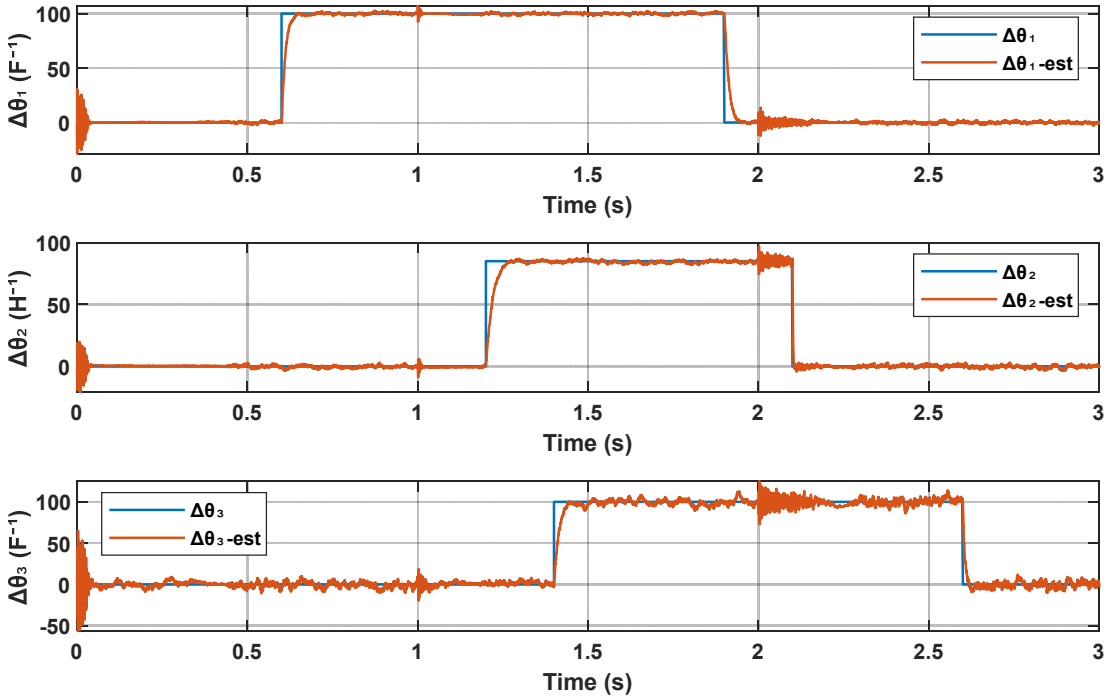


Figure 11. Comparison of actual versus estimated parameters in the second scenario.

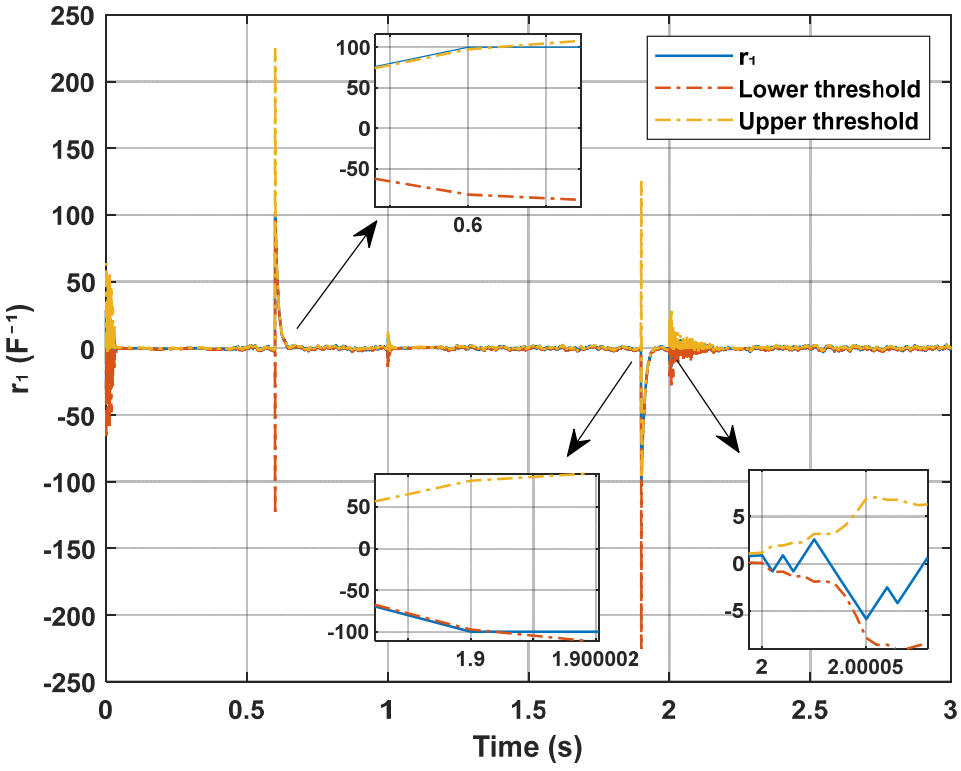


Figure 12. Residual signal of $\Delta\theta_1$ in the second scenario.

Figure 15 represents an operational translation of residuals into multiple simultaneous alerts. The system generates three separate alarms that activate and deactivate according to the precise fault chronology, demonstrating its ability to provide a complete health map in real time, even in the face of multiple concurrent failures.

Figure 16 highlights the system's performance and resilience. The results confirm that the control strategy effectively maintains operation at the maximum power point (MPP).

Even in the presence of a fault or change in radiation, the output power recovers quickly and stabilizes at the optimal power level.

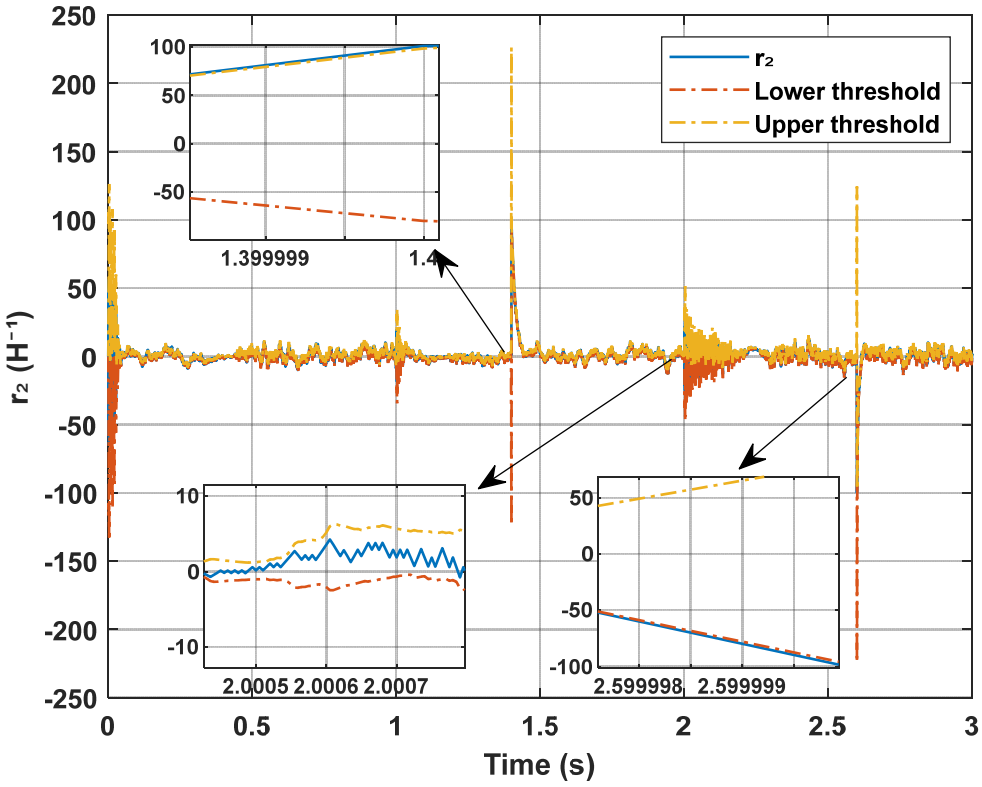


Figure 13. Residual signal of $\Delta\theta_2$ in the second scenario.

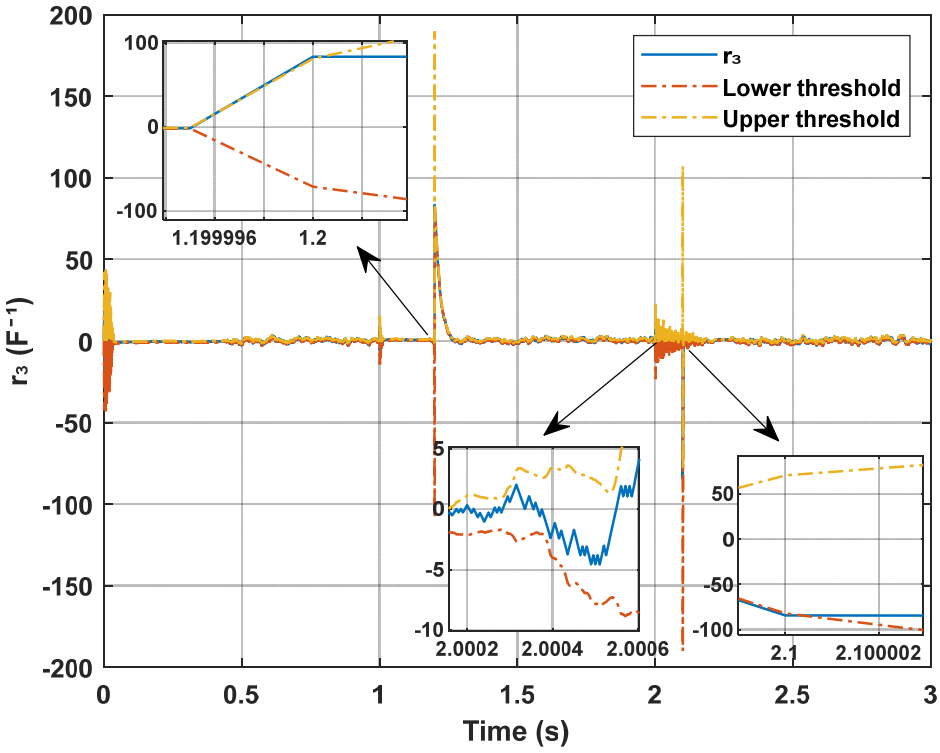


Figure 14. Residual signal of $\Delta\theta_3$ in the second scenario.

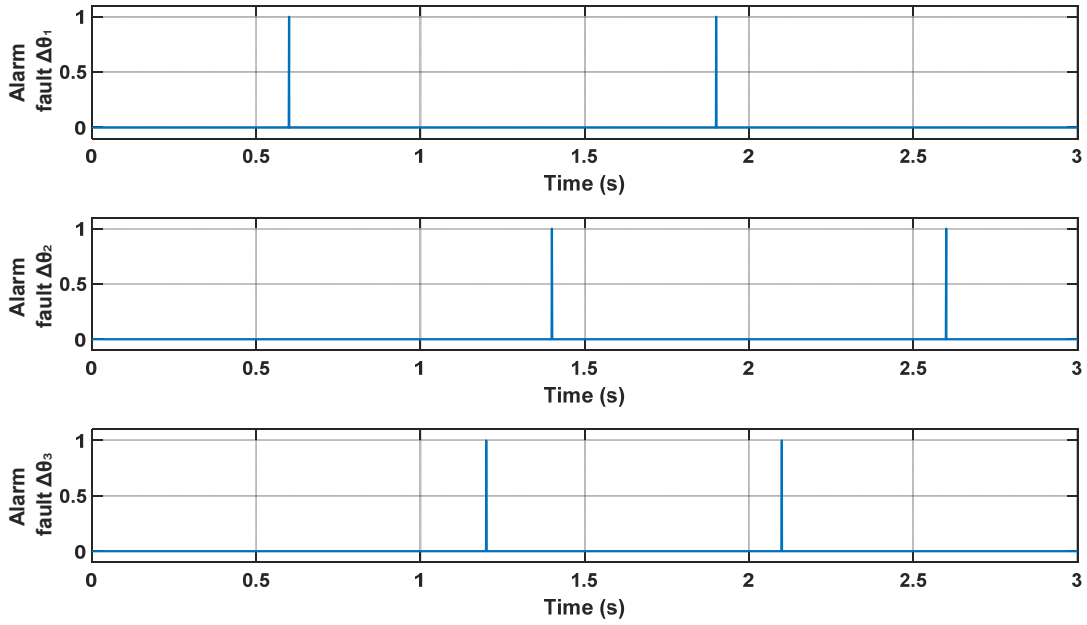


Figure 15. Fault detection in the second scenario.

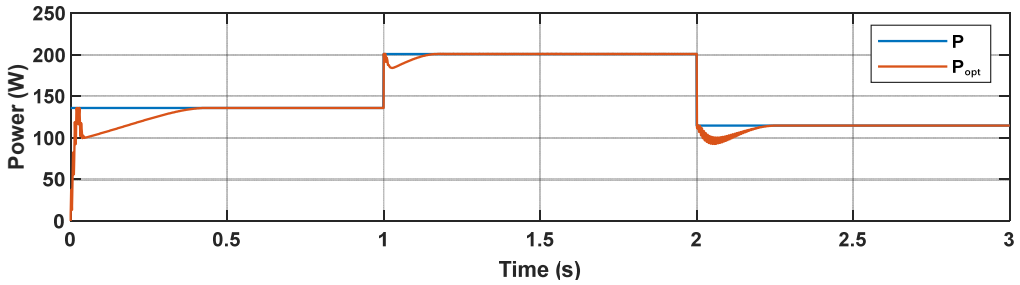


Figure 16. Evolution of the PV power and its optimal value in the second scenario.

5.1. Comparative Analysis with a Standard Sliding Mode Observer

To assess the advantages of the proposed approach, a direct comparison was made with a conventional Sliding Mode Observer (SMO) with fixed thresholds. This baseline SMO shares the same structure and gains as the proposed ASMO. Both observers were assessed under the challenging sequential fault and irradiance variation profile of Scenario 2. The performance was evaluated in terms of Average Detection Time and Number of False Alarms.

A comprehensive comparative analysis was conducted to evaluate the proposed ASMO + EWMA method against established approaches. When compared to a standard Sliding Mode Observer with fixed thresholds which illustrated in Figure 17, our approach demonstrated clear performance advantages. The standard SMO produced false alarms and showed slower detection times. In contrast, our ASMO + EWMA method achieved perfect isolation accuracy with zero false alarms and reduced detection times, representing an improvement over the standard SMO. As a conclusion, the results obtained quantitatively validate the advantages of our adaptive thresholding mechanism and enhanced observer design in handling real-world transient conditions while maintaining reliable fault detection.

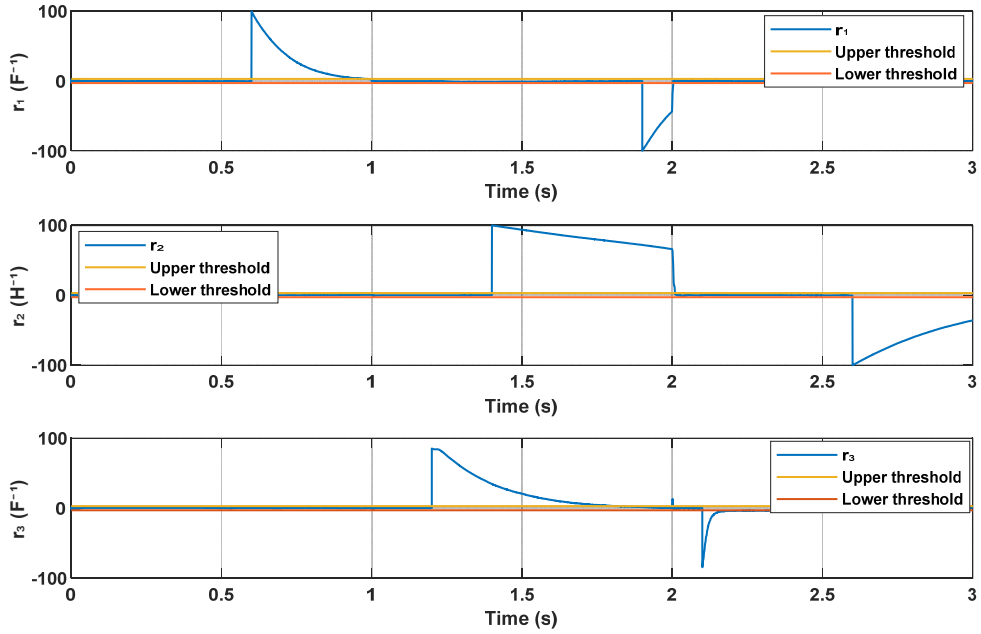


Figure 17. Residual signals obtained using SMO with fixed threshold.

5.2. Analysis of Observer Gains

To investigate the robustness of the proposed method to gain variations, a sensitivity analysis was conducted by varying the observer gains during the first fault scenario only fault in θ_1 during [0.5 s, 0.9 s]. The nominal gain configuration in Table 2 was compared with a reduced gain.

The results of the observer gain sensitivity analysis, demonstrate the impact of gain settings on detection performance. With the nominal configuration, the average detection time is 0.05 ± 0.01 s with no false alarms. When the reduced gains show that the detection time increases by approximately 50% to 0.1 ± 0.02 s, while maintaining zero false alarms as illustrated in Figure 18.

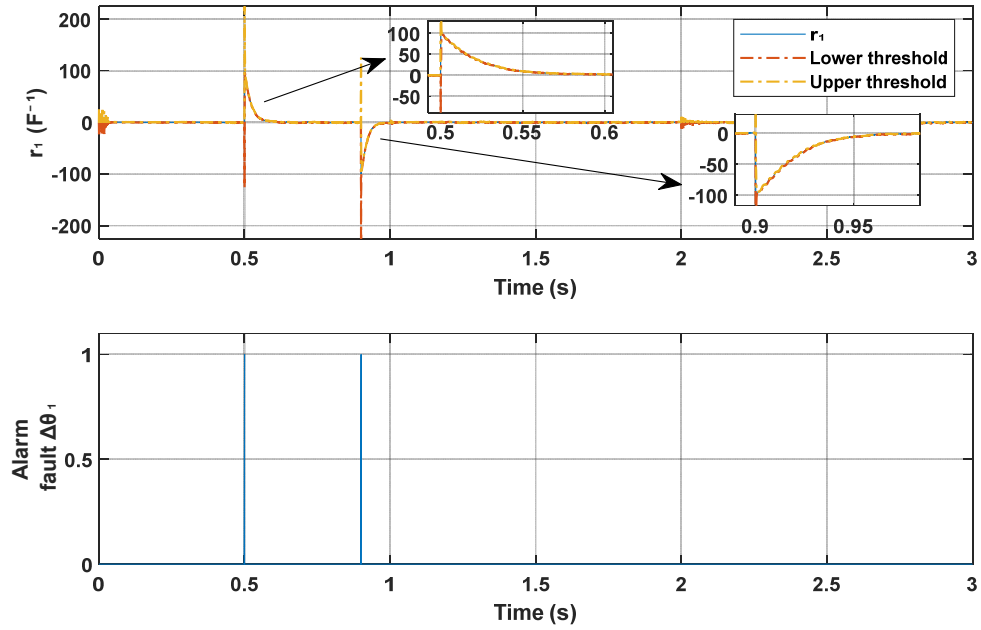


Figure 18. Residual signal of $\Delta\theta_1$ and fault detection with reduced gain.

6. Conclusions

This work presented a robust methodology for parametric fault diagnosis in photovoltaic systems, more specifically in DC-DC boost converters. We developed a unified diagnostic architecture that synergistically integrates an ASMO with a real-time detection system. The ASMO design represents a significant advancement over conventional observers. It combines the intrinsic robustness of the sliding mode against uncertainties with an online parametric adaptation capability. A notable innovation lies in the implementation of adaptive thresholds based on the EWMA approach. This approach allows effective differentiation between true faults and normal transient variations. It significantly reduces the risk of false alarms while maintaining high detection sensitivity. The dynamic adaptation of thresholds according to the system operational profile ensures optimal diagnostic performance under various operating conditions. Furthermore, comprehensive validation scenarios demonstrate the effectiveness of the overall approach. These scenarios include sequential and simultaneous faults under variable illumination conditions, highlighting the adaptive thresholding mechanism.

The simulated results confirm rapid detection capability and isolation specificity. This holds even in critical situations with multiple overlapping faults, where EWMA thresholds play a crucial role in fault discrimination.

Future research will focus on several promising directions: (1) experimental validation through hardware implementation and real-time simulation; (2) extending the methodology to cover switch and sensor faults; (3) integrating machine learning techniques to enhance fault prediction and classification; (4) applying the approach to complex multi-converter PV systems; and (5) developing self-tuning observer gains for varying operating conditions; and (6) developing active fault tolerance strategies to maintain system performance even under degraded conditions. These steps will further enhance the industrial applicability of the proposed diagnostic framework.

Author Contributions: Conceptualization, M.I. and K.D.; methodology, M.I.; software, M.I. and K.D.; validation, F.T., T.D. and M.C.; formal analysis, M.I., K.D. and F.T.; investigation, M.I., K.D. and F.T.; resources, M.I. and K.D.; data curation, F.T., T.D. and M.C.; writing—original draft preparation, M.I.; writing—review and editing, M.I., K.D. and F.T.; visualization, F.T., T.D. and M.C.; supervision, K.D. and F.T. All authors have read and agreed to the published version of the manuscript.

Funding: Prof. Tadeo was partially funded by Ministerio de Ciencia, Innovación y Universidades: MCIN/AEI/10.13039/501100011033/FEDER, UE (PID2021-123654OB-C31).

Data Availability Statement: Data generated in the simulations are available from the authors on reasonable request.

Conflicts of Interest: The authors declare no conflicts of interest.

References

1. Mariani, V.; Adinolfi, G.; Buonanno, A.; Ciavarella, R.; Ricca, A.; Sorrentino, V.; Graditi, G.; Valenti, M. A Survey on Anomalies and Faults That May Impact the Reliability of Renewable-Based Power Systems. *Sustainability* **2024**, *16*, 6042. [CrossRef]
2. Molęda, M.; Małysiak-Mrozek, B.; Ding, W.; Sunderam, V.; Mrozek, D. From Corrective to Predictive Maintenance—A Review of Maintenance Approaches for the Power Industry. *Sensors* **2023**, *23*, 5970. [CrossRef] [PubMed]
3. Pourshahbaz, N.; Eskandari, A.; Milimonfared, J.; Aghaei, M. Current-Based Fault Detection of Photovoltaic Systems. In Proceedings of the 2023 14th Power Electronics, Drive Systems, and Technologies Conference (PEDSTC), Babol, Iran, 31 January–2 February 2023; pp. 1–6.
4. Pérez-Briceño, C.; Ponce, P.; Mei, Q.; Fayek, A.R. A Type-2 Fuzzy Logic Expert System for AI Selection in Solar Photovoltaic Applications Based on Data and Literature-Driven Decision Framework. *Processes* **2025**, *13*, 1524. [CrossRef]
5. Khan, S.S.; Wen, H. A Comprehensive Review of Fault Diagnosis and Tolerant Control in DC-DC Converters for DC Microgrids. *IEEE Access* **2021**, *9*, 80100–80127. [CrossRef]

6. Lipu, M.S.H.; Faisal, M.; Ansari, S.; Hannan, M.A.; Karim, T.F.; Ayob, A.; Hussain, A.; Miah, M.S.; Saad, M.H.M. Review of Electric Vehicle Converter Configurations, Control Schemes and Optimizations: Challenges and Suggestions. *Electronics* **2021**, *10*, 477. [CrossRef]
7. Sarig, E.; Evzelman, M.; Peretz, M.M. Analog Frontend for Big Data Compression and Instantaneous Failure Prediction in Power Management Systems. *Electronics* **2025**, *14*, 641. [CrossRef]
8. Ma, J.; Zhang, L. A Deploying Method for Predicting the Size and Optimizing the Location of an Electric Vehicle Charging Stations. *Information* **2018**, *9*, 170. [CrossRef]
9. Shokoohi, S.; Moshtagh, J. Beyond Signal Processing: A Model-Based Luenberger Observer Approach for Accurate Bearing Fault Diagnosis. *AUT J. Electr. Eng.* **2024**, *57*, 163–184. [CrossRef]
10. Arena, F.; Collotta, M.; Luca, L.; Ruggieri, M.; Termine, F.G. Predictive Maintenance in the Automotive Sector: A Literature Review. *MCA* **2021**, *27*, 2. [CrossRef]
11. Givi, H.; Farjah, E.; Ghanbari, T. A Comprehensive Monitoring System for Online Fault Diagnosis and Aging Detection of Non-Isolated DC–DC Converters' Components. *IEEE Trans. Power Electron.* **2019**, *34*, 6858–6875. [CrossRef]
12. Lin, Q.; Chen, S.; Lin, C.-M. Parametric Fault Diagnosis Based on Fuzzy Cerebellar Model Neural Networks. *IEEE Trans. Ind. Electron.* **2019**, *66*, 8104–8115. [CrossRef]
13. Venkateswaran, M.; Govindaraju, C.; Santhosh, T.K. Integrated Predictive Control and Fault Diagnosis Algorithm for Single Inductor-Based DC-DC Converters for Photovoltaic Systems. *Circuit World* **2020**, *47*, 105–116. [CrossRef]
14. Nalina, B.S.; Kamaraj, V.; Babu, M.R. Fault Detection and Identification Strategy Based on Luenberger Observer for Bidirectional Interleaved Switched—Capacitor DC–DC Converter Interfaced Microgrids. *J. Electr. Eng. Technol.* **2022**, *17*, 2329–2338. [CrossRef]
15. Kimura, T.; Maruta, H. Parameter Estimation of DC-DC Converters for Failure Detection Based on Linear Approximation Model. In Proceedings of the 2021 IEEE 30th International Symposium on Industrial Electronics (ISIE), Kyoto, Japan, 20 June 2021; pp. 1–6.
16. Vinod; Kumar, R.; Singh, S.K. Solar Photovoltaic Modeling and Simulation: As a Renewable Energy Solution. *Energy Rep.* **2018**, *4*, 701–712. [CrossRef]
17. Borja-Jaimes, V.; Adam-Medina, M.; López-Zapata, B.Y.; Vela Valdés, L.G.; Claudio Pachecano, L.; Sánchez Coronado, E.M. Sliding Mode Observer-Based Fault Detection and Isolation Approach for a Wind Turbine Benchmark. *Processes* **2021**, *10*, 54. [CrossRef]
18. Sahraoui, H.; Mellah, H.; Mouassa, S.; Jurado, F.; Bessaad, T. Lyapunov-Based Adaptive Sliding Mode Control of DC–DC Boost Converters Under Parametric Uncertainties. *Machines* **2025**, *13*, 734. [CrossRef]
19. Hong, J.; Yang, J.; Liang, F.; Li, M.; Wang, F. An Adaptive Threshold Strategy Based on Empirical Distribution Functions and Information Entropy for Battery Abnormal Diagnosis and Fault Alarm. *Energy* **2025**, *332*, 135980. [CrossRef]
20. Li, X.; Lyu, M.; Gao, X.; Yuan, C.; Zhen, D. An Adaptive Threshold Method for Multi-Faults Diagnosis of Lithium-Ion Batteries Based on Electro-Thermal Model. *Measurement* **2023**, *222*, 113671. [CrossRef]
21. Attar, A.A.; Fabarisov, T.; Hagenmeyer, V.; Morozov, A. Improving Anomaly Detection with Adaptive Dynamic Threshold: A Review and Enhanced Method. In Proceedings of the 2024 8th International Conference on System Reliability and Safety (ICSRS), Sicily, Italy, 20–22 November 2024. [CrossRef]
22. Javed, H.; Ismail, M.; Saeed, N. New Extended Exponentially Weighted Moving Average Control Chart for Monitoring Process Mean. *Heliyon* **2024**, *10*, e34424. [CrossRef] [PubMed]

Disclaimer/Publisher's Note: The statements, opinions and data contained in all publications are solely those of the individual author(s) and contributor(s) and not of MDPI and/or the editor(s). MDPI and/or the editor(s) disclaim responsibility for any injury to people or property resulting from any ideas, methods, instructions or products referred to in the content.